Cold electrons at a weakly outgassing comet

P. Stephenson, M. Galand, J. Deca, P. Henri

Monthly Notices of the ROYAL ASTRONOMICAL SOCIETY

MNRAS **529,** 2854–2865 (2024) https://doi.org/10.1093/mnras/stae695
Advance Access publication 2024 March 8

Cold electrons at a weakly outgassing comet

P. Stephenson [1,2]★ M. Galand [2] J. Deca[3] and P. Henri [4,5]

[1]*Lunar and Planetary Laboratory, University of Arizona, Tucson, AZ, 85721, USA*
[2]*Department of Physics, Imperial College London, London,SW72AZ, UK*
[3]*Laboratory for Atmospheric and Space Physics, University of Colorado, , Boulder, CO, 80303,USA*
[4]*Lagrange, OCA, CNRS, UCA, Nice, 34229, France*
[5]*LPC2E, CNRS, Orleans, 45701, France*

Accepted 2024 February 23. Received 2024 February 22; in original form 2023 October 1

ABSTRACT

Throughout the Rosetta mission, cold electrons (<1 eV) were measured in the coma of comet 67P/Churyumov–Gerasimenko. Cometary electrons are produced at ∼10 eV through photoionization or through electron-impact ionization collisions. The cold electron population is formed by cooling the warm population through inelastic electron–neutral collisions. Assuming radial electron outflow, electrons are collisional with the neutral gas coma below the electron exobase, which only formed above the comet surface in near-perihelion high-outgassing conditions ($Q > 3 \times 10^{27}\,s^{-1}$). However, the cold population was identified at low outgassing ($Q < 10^{26}\,s^{-1}$), when the inner coma was not expected to be collisional. We examine cooling of electrons at a weakly outgassing comet, using a 3D collisional model of electrons at a comet. Electron paths are extended by trapping in an ambipolar electric field and by gyration around magnetic field lines. This increases the probability of electrons undergoing inelastic collisions with the coma and becoming cold. We demonstrate that a cold electron population can be formed and sustained, under weak outgassing conditions ($Q = 10^{26}\,s^{-1}$), once 3D electron dynamics are accounted for. Cold electrons are produced in the inner coma through electron–neutral collisions and transported tailwards by an $\mathbf{E} \times \mathbf{B}$ drift We quantify the efficiency of trapping in driving electron cooling, with trajectories typically 100 times longer than expected from ballistic radial outflow. Based on collisional simulations, we define an estimate for a region where a cold electron population can form, bounded by an electron cooling exobase. This estimate agrees well with cold electron measurements from the Rosetta Plasma Consortium.

Key words: Comets:general – Comets: individual: 67P/CG.

1 INTRODUCTION

A comet comprises a solid nucleus, surrounded by an envelope of partially ionized gas, known as the coma. As the comet approaches perihelion, the outgassing of ices from near the nucleus' surface increases and the coma becomes denser. The neutral gas surrounding the comet can be ionized by several processes. First, in photoionization, extreme ultraviolet (EUV) photons are absorbed by neutral molecules leading to the release of a photoelectron and an ion (Heritier et al. 2017). Secondly, energetic electrons can collide with a neutral molecule in electron-impact ionization, releasing a secondary electron and an ion (Stephenson et al. 2023). Additionally, solar wind ions can collide with the coma, generating new cometary ions through charge exchange (Simon Wedlund et al. 2019).

The electron population at a comet is not a single thermalized population. During the flybys of highly outgassing comets, such as Halley (outgassing rate $Q = 10^{30}\,s^{-1}$; Krankowsky et al. 1986) and 21P/Giacobini–Zinner ($Q = 3 \times 10^{28}\,s^{-1}$; Cowley et al. 1987), several distinct populations were measured, namely a cold (<1 eV), warm (10–15 eV) and hot population (>20 eV; Bame et al. 1986; Meyer-Vernet et al. 1986; Zwickl et al. 1986). These populations were also identified and measured throughout the Rosetta mission, even at much lower outgassing rates ($Q > 10^{26}\,s^{-1}$; Clark et al. 2015; Broiles et al. 2016a, b, Myllys et al. 2019, Wattieaux et al. 2020). They were measured by instruments of the Rosetta Plasma Consortium (RPC; Carr et al. 2007), particularly the Ion and Electron Sensor (RPC/IES; Burch et al. 2007), Langmuir Probe (RPC/LAP; Eriksson et al. 2007) and Mutual Impedance Probe (RPC/MIP; Trotignon et al. 2007). Although, similar populations were observed in low-to-intermediate and high outgassing, the origin of the populations may be quite different between the two regimes.

Over the whole outgassing range, the warm population at 67P was always detected (Myllys et al. 2019). It is composed of newly born cometary electrons, produced through either photoionization or electron impact ionization. At large heliocentric distances, electron-impact ionization was the dominant source of cometary electrons at 67P (Galand et al. 2016; Heritier et al. 2018; Stephenson et al. 2023). Close to perihelion, electron-impact ionization was weaker and photoionization was the dominant electron source (Stephenson et al. 2023).

The suprathermal electrons at comet 67P, comprising the hot and warm electron populations, were non-Maxwellian and can be better described by a combination of two kappa distributions (Broiles et al.

★ E-mail: pstephenson@arizona.edu

2016a, b; Myllys et al. 2019). However, the kappa distributions were often not sufficient to describe the suprathermal electrons measured by RPC/IES, with poor fits for 80 per cent of the measurements when away from perihelion (Myllys et al. 2019). The hot population at comet 67P has been identified as core solar wind electrons that have undergone heating in the cometary environment (Myllys et al. 2019).

At the high outgassing rates of Halley during the Giotto flyby ($Q = 10^{30}$ s^{-1}; Krankowsky et al. 1986), the hot electrons (>20 eV) in the coma have been heated as they passed through the bowshock (Rème et al. 1986; Thomsen et al. 1986; Gan & Cravens 1990), with some additional heating from wave–particle interactions (Shapiro et al. 1999). For weak outgassing, a bow shock does not form upstream of the nucleus, and the solar wind electrons are instead accelerated by an ambipolar electric field (Deca et al. 2017, 2019; Stephenson et al. 2022, 2023).

The ambipolar field forms a potential well around the comet nucleus (Divin et al. 2020), in opposition to the radial separation of cometary ions and electrons. This potential accelerates solar wind electrons by hundreds of electron volts (Nilsson et al. 2022; Stephenson et al. 2022) and funnels electrons towards the coma, increasing the likelihood that they ionize the cometary neutrals. This acceleration and deflection of electrons drove high electron-impact ionization frequencies when 67P was far from perihelion (heliocentric distance $r_h > 2$ au; Stephenson et al. 2023).

Cold electrons were observed throughout the Rosetta mission, even at very low outgassing rates ($Q < 5 \times 10^{26}$ s^{-1}; Eriksson et al. 2017; Gilet et al. 2017, 2020; Engelhardt et al. 2018; Wattieaux et al. 2020). Cold electrons are produced by cooling the warm electron population from ~10 eV, through inelastic collisions with the neutral gas at 0.01 eV (Gulkis et al. 2015). At high outgassing rates ($Q > 10^{28}$ s^{-1}), the electrons are efficiently cooled while they flow approximately radially away from the nucleus in the diamagnetic cavity (Meyer-Vernet et al. 1986; Cravens 1987; Körösmezey et al. 1987; Gan & Cravens 1990). At 67P, the cold population was expected to form in the inner coma around perihelion (Mandt et al. 2016). However, the cold electrons were still detected at outgassing rates orders of magnitude smaller, when the coma should not have been dense enough to efficiently cool them (Eriksson et al. 2017; Engelhardt et al. 2018; Gilet et al. 2020; Wattieaux et al. 2020).

Under radial outflow, the collisional region of the coma can be approximated by the electron exobase. This is where the mean free path ($\lambda = [n_n \sigma_{\rm mom}]^{-1}$) of an electron is equivalent to the scale height of the electrons ($H = \left[\frac{1}{n_e}\frac{dn_e}{dr}\right]^{-1} = r$), where $\sigma_{\rm mom}$ is the momentum transfer cross section (Mandt et al. 2016). This gives the location of the electron exobase as:

$$r = \lambda, \quad \text{where } \lambda = n_{S/C}\,\sigma_{\rm mom}\,r_{S/C}^2 = \frac{Q\,\sigma_{\rm mom}}{4\pi u_{\rm gas}} \tag{1}$$

When the exobase forms above the comet surface, some of the coma is collisional. This exobase separates inner regions dominated by collisions from outer regions dominated by transport. This is not necessarily the same region where collisional electron cooling may be expected, due to different relevant cross-sections, as cooling is caused only by inelastic processes.

The exobase estimate in equation (1) has been considered in relation to cold electron observations, and cold electrons were commonly detected far above the estimated collisional region of the coma (Engelhardt et al. 2018; Gilet et al. 2020; Wattieaux et al. 2020). Cold electrons were also frequently observed when the estimated exobase location (from equation 1) was below the comet surface. In these cases, none of the coma should have been dense enough to have significant collisions and hence to efficiently cool the warm electron population (Engelhardt et al. 2018; Gilet et al. 2020). Consequently, the current understanding of the electron cooling processes is insufficient, in the case of a weakly outgassing coma.

Electron trapping by the ambipolar potential well around the comet could provide a solution to this cooling problem. Cometary electrons, produced within the potential well, may not have enough energy to exit from the well directly into the solar wind and can become confined to a dense region of the coma (Sishtla et al. 2019; Stephenson et al. 2022). This trapping process increases the likelihood of electrons undergoing inelastic collisions and becoming cold. It is sufficient to cool some cometary electrons, but it has not been assessed quantitatively over the whole electron population. The efficiency of the trapping has not been assessed quantitatively, and it is unclear whether it is sufficient to generate cold electrons.

We aim to examine the role of the ambipolar field in enhancing the cooling of cometary electrons, at low-outgassing rates, using a 3D kinetic collisional electron model (Stephenson et al. 2022). Gan & Cravens (1990) solved the Boltzmann equation along parabolic field lines at Halley using a two-stream approach, which incorporated electron–neutral collision processes. However, at Halley (during the Giotto flyby), cold electrons made up the bulk population and could be treated as a fluid, so only the suprathermal population was addressed kinetically. At 67P, when far from perihelion, the suprathermal, warm population makes up the bulk of the electrons (Gilet et al. 2020), so a fluid approach cannot be utilized. Madanian et al. (2016) used a similar two-stream approach to reproduce observations from Rosetta, using an estimated ambipolar electric field imposed at the ends of the magnetic field lines. The two stream approach demonstrates confinement of photoelectrons and solar wind electrons in the coma (Madanian et al. 2016). However, the ambipolar field is not calculated in a self-consistent manner and is only applied at the end of the field lines. Additionally, the electron motion cannot be well captured with motion only along the field lines. In order to model electron cooling, assisted by the ambipolar electric field, it is necessary to use a fully kinetic 3D collisional model of electrons at a comet, driven by realistic electric and magnetic fields.

Electric and magnetic fields around a weakly outgassing comet have been calculated self-consistently with a fully kinetic collisionless Particle-in-Cell model (Deca et al. 2017, 2019; Divin et al. 2020). Populations of ions and electrons, from both photoionization and the solar wind, are simulated. The complex 3D fields exhibit an ambipolar potential well around the comet, and leads to trapping of particles and acceleration of the solar wind (Deca et al. 2017; Sishtla et al. 2019). However, the collisionless nature of the simulations prevents examination of the cold electron population.

We use a collisional test particle model of electrons at a comet, to examine the collisional cooling of the warm electron population (Stephenson et al. 2022). Stephenson et al. (2022) demonstrated that trapped cometary electrons undergo energy degradation in the coma, as a result of trapping in the ambipolar field, but did not focus on the cold electron population.

In this study, we focus on the cooling of warm cometary electrons through inelastic collisions, leading to the formation of the cold electron population. We also aim to demonstrate why cold electrons were frequently observed at Rosetta (Engelhardt et al. 2018; Gilet et al. 2020), when the coma of 67P was thought too rarefied to collisionally cool the cometary electrons.

In Section 2, we present the methodology used in this study, including the collisional test particle model and the simulation conditions used. In Section 3, the formation of a population of a cold

Table 1. Test particle simulations parameters. n_{SW}, $T_{SW,}$ and $u_{SW,x}$ are the number density, electron temperature, and bulk x velocity of the solar wind. $B_{SW,y}$ is the y-component of the upstream magnetic field. $\nu_{h\nu}^{ioni}$ is the photoionization frequency and $T_{h\nu}$ is the temperature of the injected photoelectron distribution. u_{gas} is the outflow velocity of the neutral coma and dx_{EB} is the resolution of the electric and magnetic fields.

Parameter		Value	Parameter		Value
n_{SW}	[cm^{-3}]	1	T_{SW}	[eV]	20
$u_{SW,x}$	[km s^{-1}]	400	$B_{SW,y}$	[nT]	6
$\nu_{h\nu}^{ioni}$	[s^{-1}]	1.12×10^{-7}	$T_{h\nu}$	[eV]	20
u_{gas}	[km s^{-1}]	1	dx_{EB}	[km]	10.7

electron population is demonstrated at low-outgassing rates. The role of the ambipolar field in driving the cooling of cometary electrons is examined in Section 4, and the location of the electron cooling exobase is assessed in the presence of the electric and magnetic fields.

2 METHODS

We model the cooling of electrons at a comet using 3-dimensional test particle simulations of electrons at a comet (Stephenson et al. 2022), at three outgassing rates: $Q = 10^{26}, 5 \times 10^{26}$, and 10^{27} s^{-1}. The test particle model incorporates electrons from three sources: the solar wind, photoionization of the neutral coma, and secondary electrons generated in electron–neutral collisions. The injected photoelectrons and solar wind electrons are sampled from a Maxwellian distribution, with the solar wind population moving with a bulk velocity of $\boldsymbol{u}_{SW} = 400\,\mathrm{km\,s^{-1}}\hat{\boldsymbol{x}}$. Once created, the electrons move in response to the electric and magnetic fields and are subject to collisions with the neutral gas coma. The particles are terminated when they leave the simulation domain, or hit the cometary nucleus. The $\hat{\boldsymbol{x}}$ direction is defined by the solar wind flow, while the $\hat{\boldsymbol{y}}$-axis is aligned with the interplanetary magnetic field ($\boldsymbol{B} = B_{SW}\hat{\boldsymbol{y}}$ at the upstream boundary). The domain has dimensions of 3000 × 3000 × 3000 km with the boundaries of x at −1200 and 1800 km and boundaries in y and z at ±1500 km.

The electric and magnetic fields are calculated using a collisionless fully kinetic particle-in-cell simulation (Deca et al. 2017, 2019), and are used as a stationary input to the electron simulation. The test particle simulations are run using the same solar wind conditions, cometary outgassing, and photoionization frequency as the PiC model (see Table 1). Key differences between the models are the electron mass and the addition of electron neutral collisions. Due to computational constraints, the PiC model uses an electron mass of $m_e = m_p/100$, whereas the true electron mass is used in the test particle model. The increased electron mass in the PiC model reduces the speed of the electrons for a given energy, and therefore makes collisions less likely to occur. It can also impact the energy variation of electrons within the domain as they move in a convective $\boldsymbol{E}$ field (Stephenson et al. 2022). As such, it is crucial to use the true electron mass to capture the collisionality within the coma.

The inclusion of collisions within the simulations can have some feedback onto the fields, which is not included in the test particle model. Reduced electron temperatures in the inner coma can weaken the ambipolar field in the region (Stephenson et al. 2022). However, the potential well is constructed over a much larger region and the depth is not significantly reduced from the collisionless case, with only a slight flattening in the potential seen around the nucleus.

The neutral coma is spherically symmetric and purely water, giving a neutral density of

$$n_{H_2O} = \frac{Q}{4\pi u_{gas} r^2}. \tag{2}$$

where u_{gas} is the neutral outflow velocity and r is the cometocentric distance. The photoelectrons are produced by ionization of the neutral coma, with a constant photoionization frequency throughout the coma. At $Q = 10^{27}$ s^{-1}, the solar flux is attenuated by less than 10 per cent close to the nucleus ($r < 10$ km), so it is reasonable to assume that the coma is optically thin throughout the domain.

The electron–neutral collisions are treated as stochastic processes, with all the relevant electron–water collision processes included: elastic scattering, inelastic excitations, and electron-impact ionization (Stephenson et al. 2022).

2.1 Density and production of cold electrons

Statistical quantities of the electron population are computed by accumulating electron trajectories (between 3 and 4 million particles for the different outgassing rates), from each of the electron populations. The base level output of the test particle model is the energy distribution function (edf), $f(\boldsymbol{x}, E)$ [cm^{-3} eV^{-1}]. This is recorded on a 100 × 80 × 80 grid centred on the comet, with the same resolution as the input electric and magnetic fields (dx_{EB}, see Table 1). The density of cold electrons ($E < 1$ eV) is given by

$$n_{e,cold}(\boldsymbol{x}) = \int_0^{1\,\mathrm{eV}} f(\boldsymbol{x}, E)\,dE. \tag{3}$$

The 1 eV threshold was the maximum temperature of the cold electron population measured during the Rosetta mission (Wattieaux et al. 2020).

The density of cold electrons is driven by the combination of production and transport of electrons in the coma. At a weakly outgassing comet, electron–ion recombination is not significant and can be neglected (Galand et al. 2016). It is useful to distinguish between regions where the cold electrons are 'produced' and those where they appear through transport. This 'production' does not relate to the generation of new electrons in the coma. It is defined as the number of electrons per unit volume and time that become cold as a result of inelastic collisions in a region. This is given by

$$P_{e,cold}(\boldsymbol{x}) = n(\boldsymbol{x}) \sum_j \int_{E_{Th,j}}^{E_{loss,j}+E_{cold}} J(\boldsymbol{x}, E)\,\sigma_j(E)\,dE, \tag{4}$$

where $\sigma_j(E)$ is the collision cross section for the process, j, at energy E. The integral is from the threshold energy of a process ($E_{Min} = E_{Th,j}$) to the maximum energy that would bring an electron to energy $E < E_{cold}$ after the collision, $E_{Max} = E_{loss,j} + E_{cold}$). The energy loss for a collision is $E_{loss,j} = E_{Th,j}$ for excitations and $E_{loss,j} = (E + E_{Th,j})/2$ for ionization collisions, where the energy is partitioned with the secondary electron. The electron particle differential flux, $J(\boldsymbol{x}, E)$, is given by:

$$J(\boldsymbol{x}, E) = f(\boldsymbol{x}, E)\sqrt{\frac{2E}{m_e}}. \tag{5}$$

We include a range of electron collisions with water, including vibrational and electronic excitations as well as ionization (see Fig. 1). The processes and their corresponding threshold energies are listed in Table 2. The cross-sections are summarized by Itikawa &

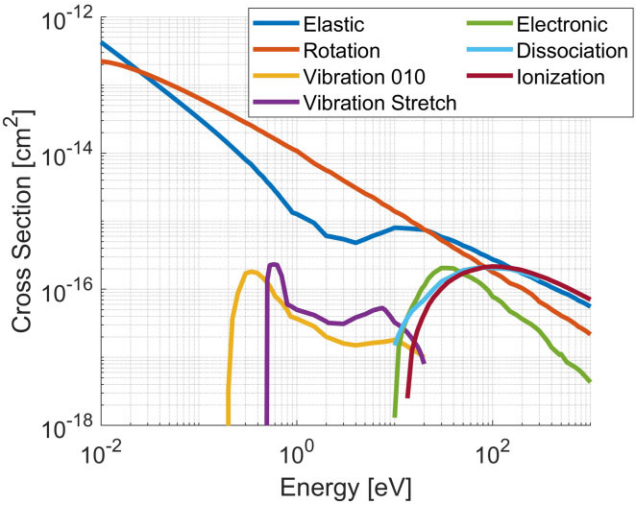

Figure 1. Cross-sections for electron impact on water included in the test particle model. Inelastic cross-sections, including ionization, are summarized by Itikawa & Mason (2005). The elastic cross-section is derived from measurements by Cho et al. (2004) and Faure et al. (2004) (see Stephenson et al. 2022). Here, the ionization collisions have been summed, but they are separately implemented in the test particle model.

Table 2. Collision processes for electron impact on water included in the test particle model, with the corresponding threshold energies $E_{\rm Th}$ (Chutjian et al. 1975; Itikawa & Mason 2005).

Collision process	Threshold energy [eV]
Elastic	0
Rotational ($J = 0 \rightarrow 1$)	0.004
Vibrational bending (010)	0.198
Vibrational stretching (100 & 001)	0.453
Electronic	10
Dissociation	7
Ionization	–
(H_2O^+, OH^+, O^+, H_2^+, H^+, O^{2+})	12.62–54.1

Mason (2005), and the threshold energy for electronic transitions is provided by Chutjian, Hall & Trajmar (1975). We also include elastic collisions, using measurements from Cho et al. (2004) and Faure, Gorfinkiel & Tennyson (2004) as outlined in Stephenson et al. (2022), but these do not directly cool electrons.

2.2 Electron depth

The electron depth, $\tau_{\rm e}$ is a useful measure of collisionality of the coma. For a given electron, this is defined as

$$\tau_{\rm e} = \sum_j \int_{\rm path} n(\boldsymbol{x})\, \sigma_j(E)\, {\rm d}s, \tag{6}$$

where the 'path' represents the full trajectory of the electron, from its birth until it leaves the simulation domain or hits the nucleus. The focus of this study is to examine the cooling of electrons within the coma, so we only calculate the electron depth for processes that cause substantial energy loss ($E_{\rm Th} > 0.15$ eV). This excludes the rotational excitations with $E_{\rm Th} > 0.004$ eV and the purely elastic collisions. These are still included in the simulations and are only removed for the post-simulation analysis of electron depths. If the electron depth is large ($\tau_{\rm e} > 1$), electrons are likely to undergo inelastic collisions and will be efficiently cooled.

3 FORMATION OF A COLD ELECTRON POPULATION

3.1 Example of a cooled electron

Fig. 2 shows an example gyroaveraged trajectory of a cometary electron that is cooled by collisions with the neutral coma at an outgassing rate of $Q = 5 \times 10^{26}$ s^{-1}. The electron is produced through photoionization of a neutral molecule in the coma at a cometocentric distance of $r = 20$ km, with an initial energy of 35.3 eV. The initial velocity largely drives gyromotion with an initial perpendicular energy of 28.5 eV (yellow, Fig. 2c). The small parallel energy (6.8 eV) means the electron is tightly confined by the ambipolar potential well in a dense region of the neutral coma. Additionally, for each step along the field line, the electron travels twice as far through its gyromotion. Within 0.25 s of its creation, the electron has built up an electron depth $\tau_{\rm e} > 2$, increasing to $\tau_{\rm e} > 5$ if the elastic rotational cross-sections are included.

The electron is elastically scattered on several occasions, driving rotations in the velocity and redistributing the parallel and perpendicular energies. At $t = 0.1$ s, the perpendicular energy drops from 36.9 to 9.4 eV, which is shortly followed by an increase to 49.8 eV, because of scattering collisions. The electron does not have a large parallel energy for a long period, and is therefore well constrained to dense regions by the potential well. A large parallel energy can also lead to a substantial curvature drift, reducing the number of oscillations through the inner coma and boosting the rate of transport out of the collisional region.

The electron undergoes six inelastic collisions within the first 0.35 s after ionization, three of which cause dissociation of a water molecule ($E_{\rm Th} = 7$ eV). At $t = 0.26$ s, the electron ionizes a water molecule (producing H_2O^+, $E_{\rm Th} = 12.62$ eV), followed shortly by an electronic excitation ($E_{\rm Th} = 10$ eV). This combination of the ionization and electronic transition degrades the electron energy from 65.5 to 17.6 eV, and leaves a parallel energy of only 0.3 eV. The electron then gyrates rapidly with a slight $\boldsymbol{E} \times \boldsymbol{B}$ drift, before causing another ionization and falling to a total energy of 2.55 eV. The electron is then scattered elastically, such that the energy is almost entirely parallel to the magnetic field line. The electron oscillates in the potential well, losing energy as it moves to higher potentials, often spending substantial time with an energy below 1 eV. The electron does undergo further inelastic collisions with small threshold energies ($E_{\rm Th} = 0.004$, 0.198 eV), before moving downstream and towards the tail.

3.2 Cold electron density

Fig. 3 shows the cold electron density (<1 eV) for collisional simulations at all three outgassing conditions (see Table 1) in the xz-plane, i.e. the plane-perpendicular to the upstream solar wind magnetic field. In all three cases, a substantial cold electron population is observed. At the lowest outgassing rate ($Q = 10^{26}$ s^{-1}), the cold electron density reaches 0.05 cm^{-3} in the inner coma. The density decreases sharply with increasing cometocentric distance, falling to 0.02 cm^{-3} at 50 km.

A tail of cold electrons, with a density of 0.01 cm^{-3}, are observed extending from the inner coma towards $+x$ and $+z$ (see Fig. 4a). The electrons in the inner coma and in the tail structure have been cooled through collisions with the neutral coma. They are primarily

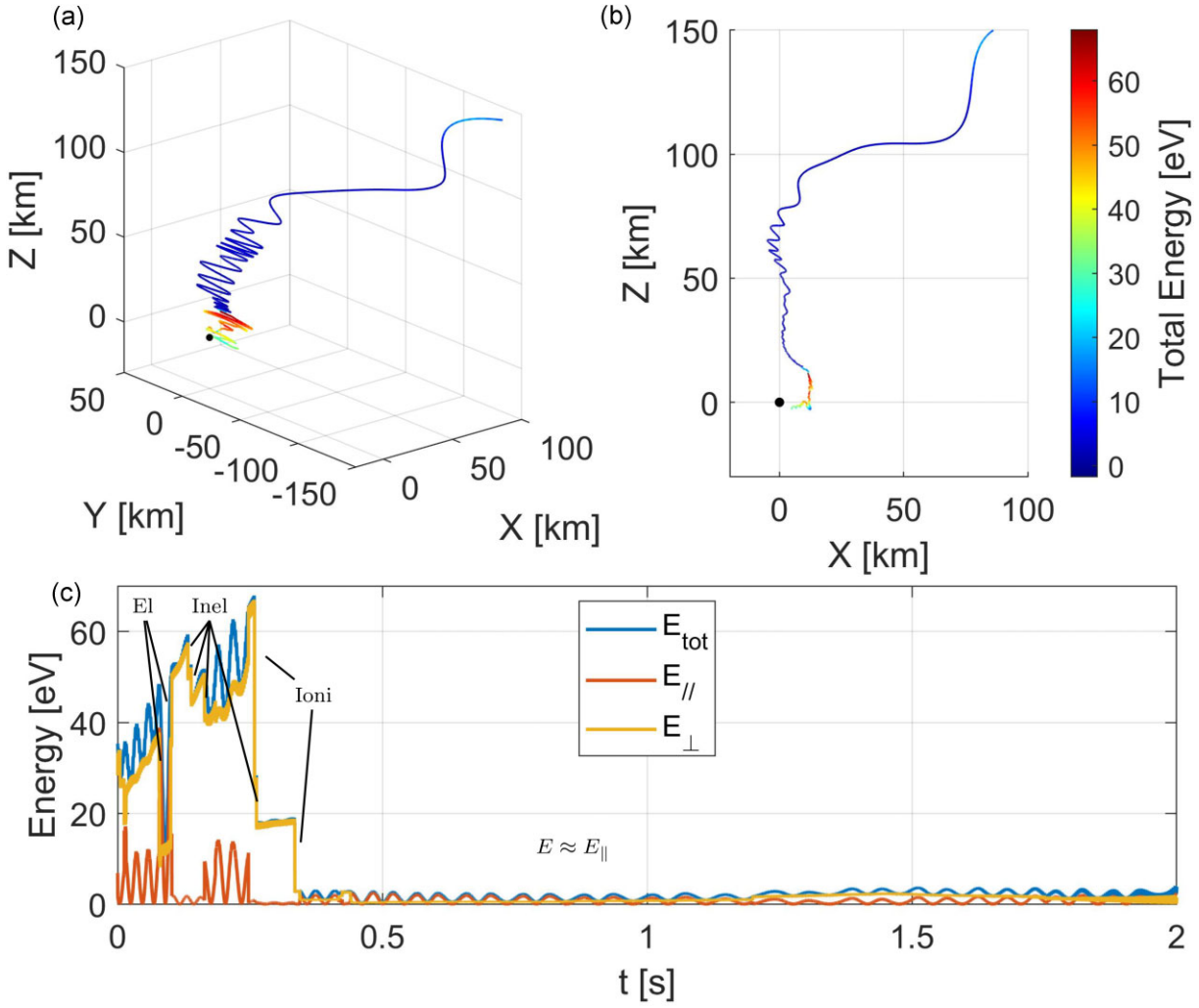

Figure 2. (a,b) Gyroaveraged trajectory of a cometary electron that is collisionally cooled at an outgassing rate of $Q = 5 \times 10^{26}\,\mathrm{s}^{-1}$. (c) Energy variation of the cometary electron as it moves through the coma. The major collisions undergone by the electron are highlighted. El – elastic. Inel – inelastic collisions excluding ionization, e.g. dissociation or electronic transitions. Ioni – electron-impact ionization.

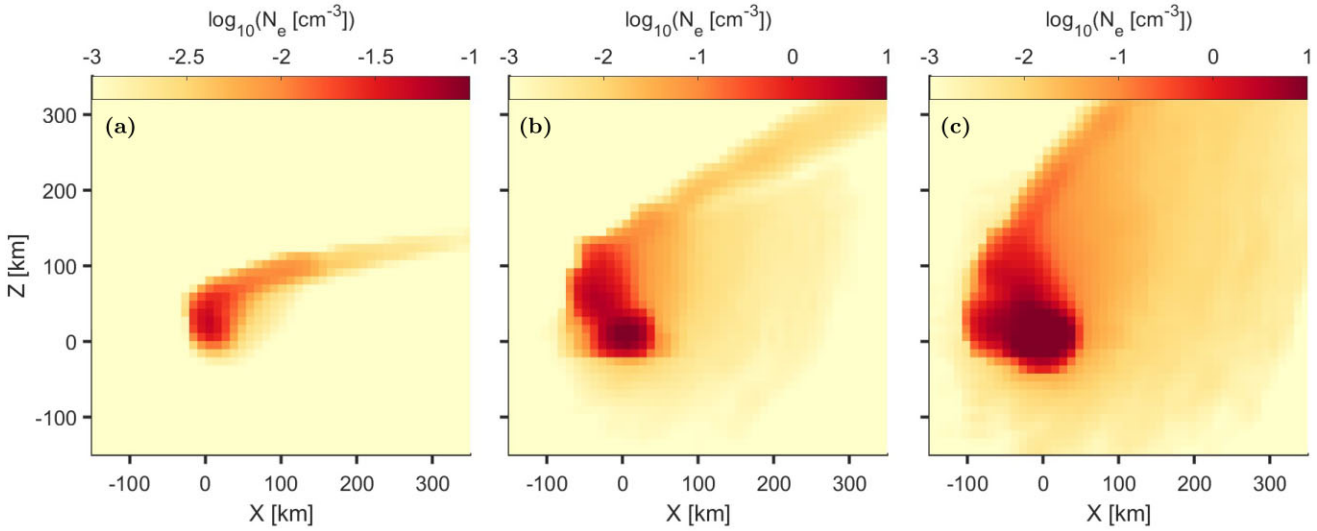

Figure 3. Cold electron density in the *xz*-plane at outgassing rates of (a) $10^{26}\,\mathrm{s}^{-1}$, (b) $5 \times 10^{26}\,\mathrm{s}^{-1}$, and (c) $10^{27}\,\mathrm{s}^{-1}$.

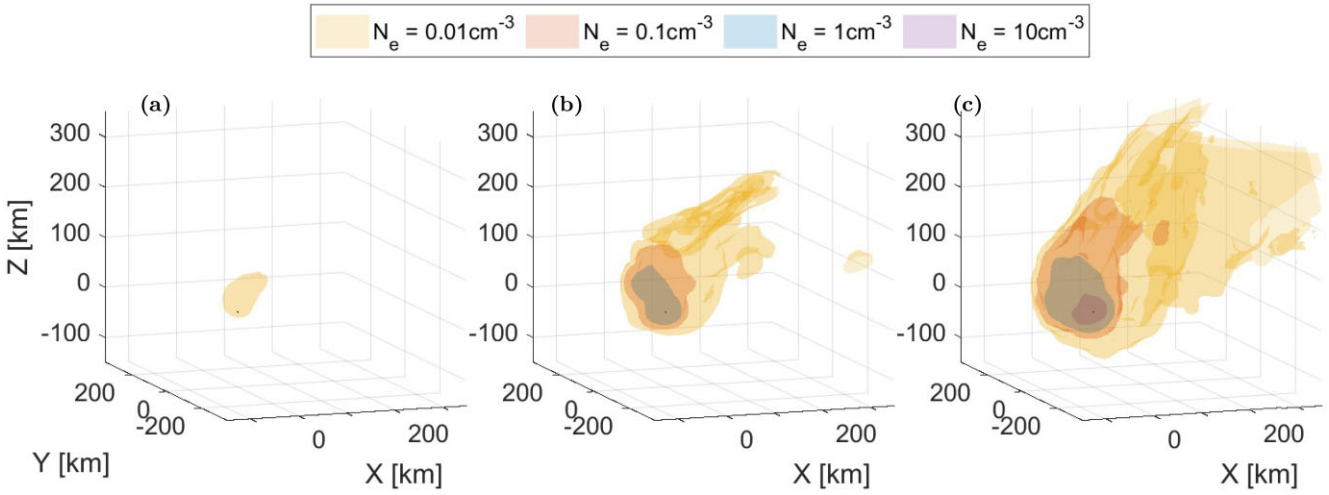

Figure 4. Surfaces of constant cold electron density (<1 eV) at outgassing rates of (a) 10^{26} s^{-1}, (b) 5×10^{26} s^{-1}, and (c) 10^{27} s^{-1}. Only the cometary electron populations are included.

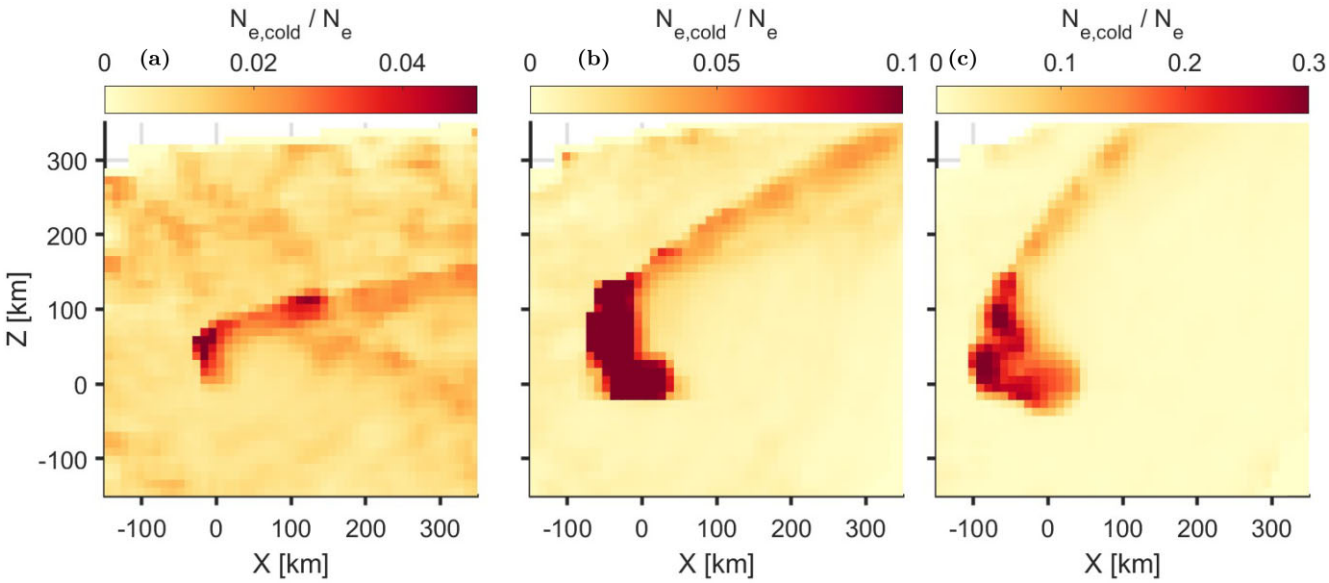

Figure 5. Fraction of electron density which constitutes cold electrons in the coma at outgassing rates of (a) 10^{26} s^{-1}, (b) 5×10^{26} s^{-1} and (c) 10^{27} s^{-1}. The range of the colour bar varies between cases.

cometary electrons, although there is some contribution from solar wind electrons that have been cooled and trapped in the ambipolar potential well (15 per cent of cold electron density).

At $Q = 5 \times 10^{26}$ s^{-1}, the dense cold electron region extends further from the nucleus (up to 70 km) and reaches a maximum density of 11.5 cm^{-3}. The asymmetry of the dense cold electron population is more pronounced towards $+z$ than in the lowest outgassing case (see Fig. 4b). The tailward region of cold electrons is very similar to the case at $Q = 10^{26}$ s^{-1}, but with an enhanced density of 0.05 cm^{-3}. The 3D shape of the extended cometary cold electron tail is shown in Fig. 4(b). The cold electron cloud is widest (along y) close to the nucleus and slightly downstream. Further downstream, the cold electron cloud becomes more tightly confined in both y and z.

At $Q = 10^{27}$ s^{-1}, the cold electron population is colder and denser than in the more weakly outgassing cases (see Fig. 3). The dense region of cold electrons also extends up to 200 km from the nucleus.

The cold electron density reaches up to 44.6 cm^{-3} in the inner coma, quickly falling to 10 cm^{-3} at 50 km and then to 2 cm^{-3} at 100 km along $+z$. The bulk of the cold electrons are of cometary origin, but 17 per cent are solar wind electrons that collide in the inner coma and become trapped in the potential well.

3.3 Fraction of cold electrons

As the (cold) electron density scales with the outgassing rate from the nucleus, it is useful to examine the fraction of electrons which are cold (see Fig. 5). At $Q = 10^{26}$ s^{-1}, the cold electrons only make up a large fraction close to the nucleus, reaching up to 10 per cent in the inner coma. Further downstream, only 3 per cent of the electron density is made up of cold electrons. As the outgassing rate increases, the cold electron fraction also rises, peaking at 13 per cent in the inner

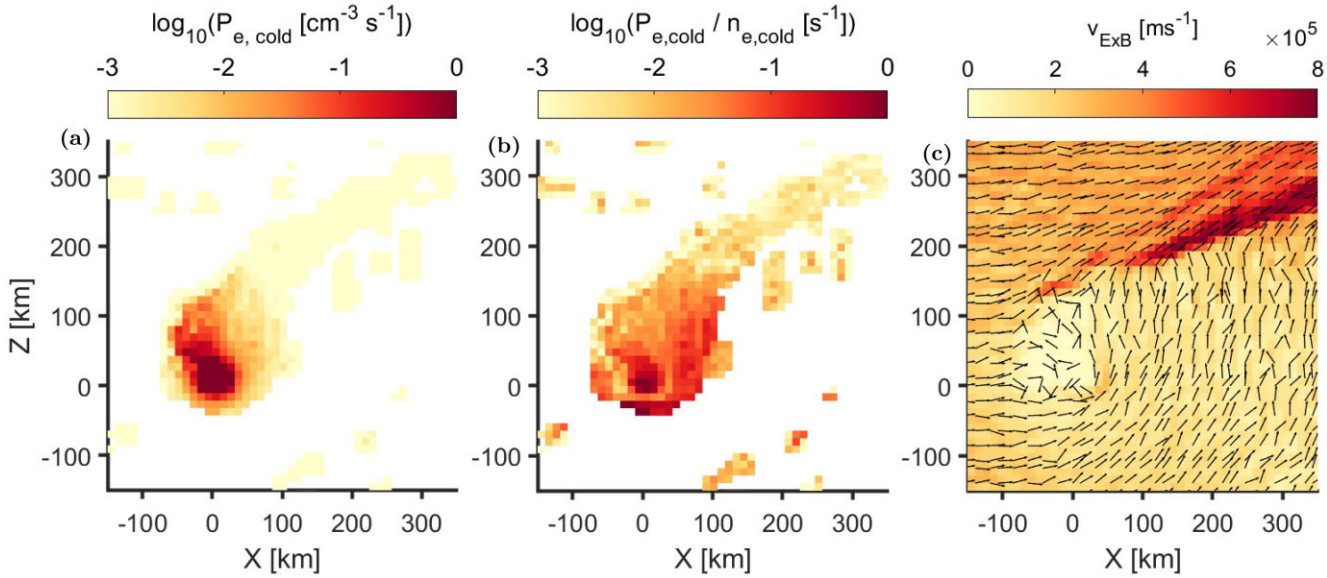

Figure 6. Source and transport of cold electrons at $Q = 5 \times 10^{26}\,s^{-1}$. (a) Cold electron production rate calculated using equation (4). (b) Ratio between the production rate and density of cold electrons. (c) $\boldsymbol{E} \times \boldsymbol{B}$ drift velocity in the xz-plane. The arrows indicate the direction of the velocity vector projected onto the plane. Regions in a and b are set as white where the cold electron density was less than 0.01 cm^{-3}.

coma for $Q = 5 \times 10^{26}\,s^{-1}$ and at 25 per cent for $Q = 10^{27}\,s^{-1}$. The fraction of cold electrons is also boosted in the tailward region, which is connected to the collisional region of the coma through transport. The increasing cold electron fraction demonstrates that the coma is increasingly collisional as the outgassing rate increases, and the increase in density is not linear with outgassing rate.

3.4 Source of cold electrons

The densities and fractions of cold electrons show the regions where cold electrons can be observed, but not where cold electrons are produced or how they are transported. Here, we examine the production of cold electrons (using equation 4) throughout the coma at $Q = 5 \times 10^{26}\,s^{-1}$ (see Fig. 6a). The production of cold electrons is defined where the electron becomes cold through inelastic collisions, as opposed to the production of electrons through ionization of neutrals.

As seen with the cold electron density in Fig. 3(b), the production of cold electrons is focused around the nucleus with an asymmetry towards $+z$. Transport from the inner coma drives electrons towards $+z$, meaning more electrons at $+z$ including those which can be cooled. Very few electrons are produced far from the nucleus, with the production rate dropping by 3 orders of magnitude within 100 km of the nucleus. This is caused by the reduction in density of both the neutral gas and electrons with cometocentric distance.

To distinguish regions where cold electrons are produced from regions of transport, Fig. 6(b) shows the ratio of cold electron production to cold electron density. Close to the nucleus, the ratio is large and cold electrons are produced at high rates. This is the 'source region' for cold electrons. Farther into the tail where cold electrons are present (see Fig. 3b), the ratio is much smaller meaning few electrons become cold locally. They instead arrive at the region through transport, from areas of higher neutral density and collisionality.

Cold electrons are driven into the tailward region via drifts set up by the electric and magnetic fields. For cold electrons, the curvature drift is small as it depends on a large parallel velocity. As such, the dominant drift mechanism is the $\boldsymbol{E} \times \boldsymbol{B}$ drift. Fig. 6(c) shows the magnitude and direction of the $\boldsymbol{E} \times \boldsymbol{B}$ drift in the xz-plane. The tailward cold electron region (see Fig. 3b) closely follows the $\boldsymbol{E} \times \boldsymbol{B}$ drift away from the inner coma. The cold electron tail also expands in the y-direction, as it moves downstream (see Fig. 7).

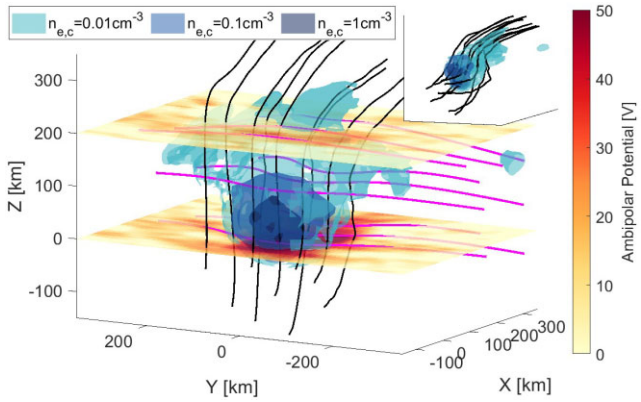

Figure 7. Cold electron density isosurfaces (blue) at an outgassing rate of $Q = 5 \times 10^{26}\,s^{-1}$. (pink) Magnetic field lines. (black) Streamlines of electrons following the $\boldsymbol{E} \times \boldsymbol{B}$-drift through the coma. The slices show the ambipolar potential well at $z = 0$ and $z = 200$ km. The inset figure shows the same isosurfaces and streamlines.

Cold electrons are produced in the inner coma through collisions with the neutral gas. Once produced, they are then transported downstream as they follow an $\boldsymbol{E} \times \boldsymbol{B}$ drift, forming a tail-like region.

4 TRAPPING AND THE ELECTRON EXOBASE

We have shown that a cold electron population can be produced and sustained in the coma of a weakly outgassing comet. In all three outgassing rates considered in Section 3, a cold electron population would not be expected to form under the assumption of radial ballistic

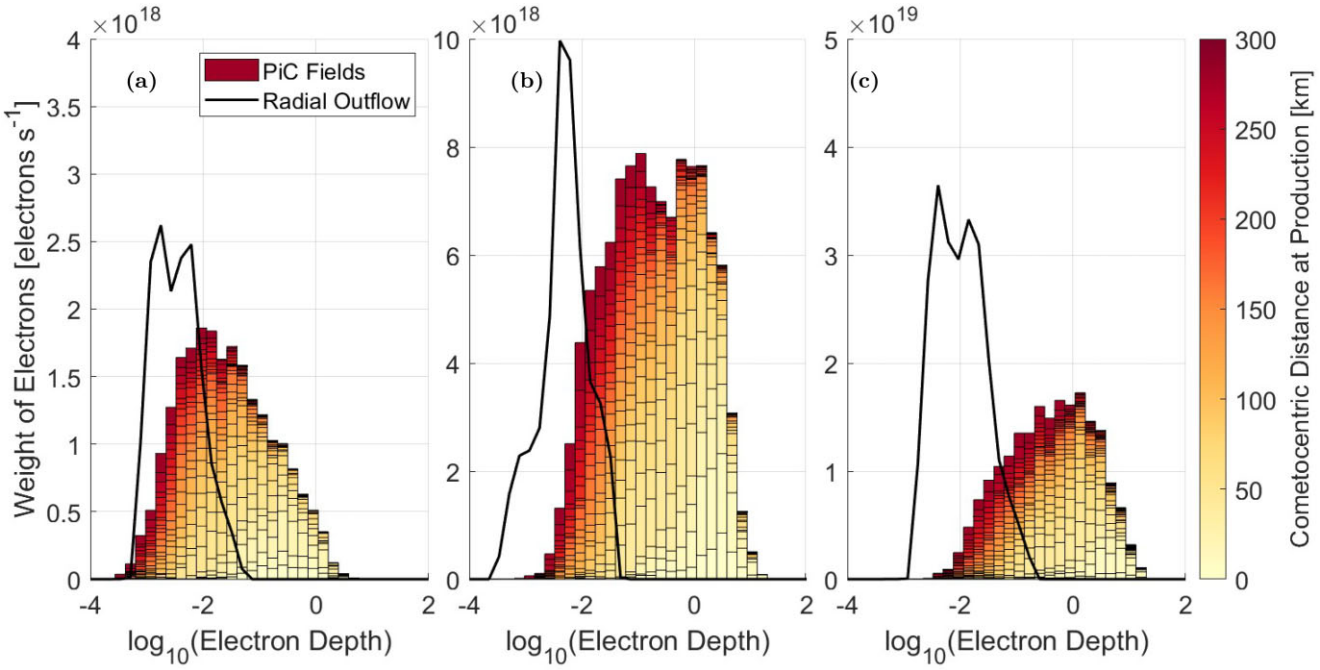

Figure 8. Electron depth distributions of cometary electrons (photoelectrons and secondary electrons) at outgassing rates of (a) 10^{26} s^{-1}, (b) 5×10^{26} s^{-1}, and (c) 10^{27} s^{-1}. The colour of the bars indicates the cometocentric distance at which the electron was initially produced in the coma. The black lines correspond to the radial outflow case, with electrons produced through photoionization.

Table 3. Properties of the electron depth, τ_e, distributions for radial outflow and with realistic electric and magnetic fields. The electron exobase estimates are based on exponential fits to the collisional electron fraction in Fig. 9.

Outgassing rate [s^{-1}]	Median τ_e radial outflow	Median τ_e PiC fields	Collisional electron percentage [%]	Revised electron exobase radius [km]
10^{26}	2.7×10^{-3}	1.5×10^{-2}	1.9	5
5×10^{26}	4.0×10^{-3}	1.4×10^{-1}	20	65
10^{27}	7.5×10^{-3}	3.3×10^{-1}	28	105

cometary plasma transport. In order to demonstrate the impact of the gyromotion and trapping of electrons in the ambipolar electric field, we have calculated the electron depth (see equation 6) for each of the simulated particles, under radial outflow and using the realistic 3D electric and magnetic fields. We only include cometary electrons in the distributions as the prior assumption of radial outflow cannot be applied to solar wind electrons, and cometary electrons are more likely to form the cold population (see Section 3.2).

Fig. 8 shows the distribution of electron depths for the outgassing rates of (a) $Q = 10^{26}$, (b) $Q = 5 \times 10^{26}$, and (c) $Q = 10^{27}$, under radial outflow (black lines) and with realistic fields (coloured bars). The electrons modelled with realistic fields have been stratified by the cometocentric distance at which the electrons were produced through ionization.

Under the previously assumed case of radial outflow, no cometary electrons were expected to become collisional for all three outgassing rates. Even at the highest considered outgassing rate of $Q = 10^{27}$ s^{-1}, 98 per cent of the electrons traced electron depths less than 0.1, and are therefore very unlikely to undergo inelastic collisions and form a cold electron population.

With the electric and magnetic fields from the PiC simulation, electrons undergo much larger electron depths and are far more likely to collide than in the case of radial outflow. The median electron depths increased by a factor of 6–50 relative to radial outflow under the same outgassing conditions (see Table 3). The upper quartiles of the electron depth increased by a larger factor of 15–100 relative to radial outflow.

The increase in the electron depth arises from the extended path traced out by the electrons as they are subject to the electric and magnetic fields. The combination of gyration around the magnetic field lines with trapping in the ambipolar potential well greatly increases the distances electrons travel. Additionally, electrons trapped by the ambipolar field bounce back and forth in the potential well, passing multiple times through dense regions of the coma where the potential well is deepest. This further amplifies the likelihood of electrons undergoing inelastic collisions.

The widths of the electron depth distributions are also enhanced compared to the case of radial outflow. With realistic fields, there is substantially more variety in the paths and energies that electrons can trace out. Some electrons very quickly leave the cometary environment, moving approximately parallel to the magnetic field lines and out of the simulation. These electrons make up the smallest electron depths, while electrons produced close to the nucleus with a velocity approximately perpendicular to the magnetic field lines are more likely to experience a large electron depth.

The electron depth distribution shifted to larger depths at higher outgassing rates, with the median electron depth increasing from 0.0154 at $Q = 10^{26}$ s^{-1} to 0.327 at $Q = 10^{27}$ s^{-1}. The percentage of cometary electrons that had large electron depths also increased with the outgassing rate, rising from 1.9 to 28 per cent at $Q = 10^{27}$ s^{-1}. As

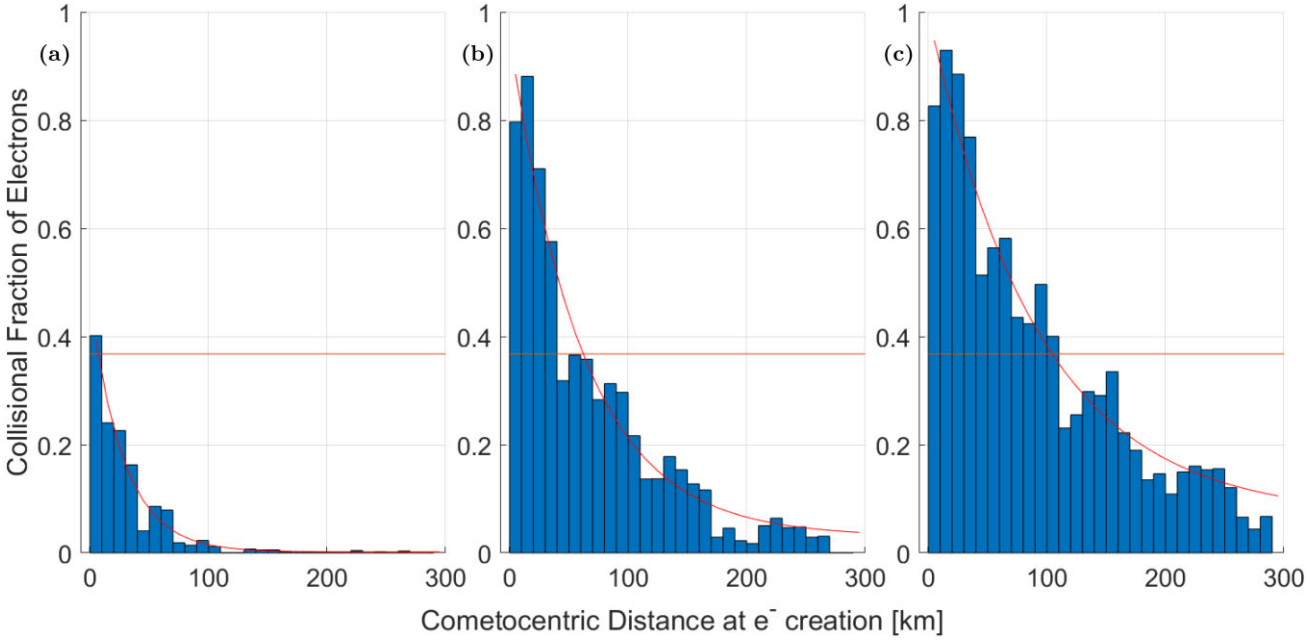

Figure 9. Fraction of electrons with an electron depth $\tau_e > 1$, among all electrons initially produced at a given cometocentric distance (in 10 km bins) through photoionization or electron-impact ionization. (a) $Q = 10^{26}\,s^{-1}$, (b) $Q = 5 \times 10^{26}\,s^{-1}$, and (c) $Q = 10^{27}\,s^{-1}$. The fits to the collisional fraction are shown by red lines.

expected, this shows that the coma becomes increasingly collisional with larger outgassing rates and the electron population becomes a larger fraction of the total electrons as seen in Fig. 5.

The electron depth distributions also skew further to higher electron depths with increasing outgassing rates. There is an apparent cutoff at an electron depth of $\tau_e = 10$. This is due to the threshold energy 0.198 eV of the processes included in the electron depths. At very large depths ($\tau_e > 10$), the electron is likely to have undergone numerous collisions and become collisionally cooled. The electrons can still undergo further collisions that are elastic or involve rotational transitions ($E_{Th} = 0.004$ eV), but these contribute little additional cooling of the electron.

The largest electron depths are experienced by electrons produced close to the nucleus, where the neutral density is largest. These electrons are also more likely to be produced deeper in the ambipolar potential well and undergo trapping. Electrons produced at the same cometocentric distance have a wide spread in the resulting electron depths, exceeding several orders of magnitude. The range of depths originates from two sources: the energy variation of the electrons and the variety in the electron trajectory. The inelastic collision cross-section varies by a factor of 20 between energies of 2 and 50 eV, so electrons produced at different initial energies may have quite different electron depths. Even for a given cometocentric distance, the position and velocity direction of the electron can lead to widely differing trajectories. One electron may have a small parallel velocity and be trapped within the ambipolar potential, while another may easily escape the potential and quickly leave the cometary environment without passing through the dense near-nucleus region.

4.1 Electron cooling exobase

The electron exobase separates the collisional and non-collisional regions of the coma. With realistic fields, the electron depths experienced by electrons are significantly larger than under the assumed case of radial outflow. As such, it is worth revisiting the definition of the exobase to better assess where this boundary lies.

An electron can be considered collisional if it traces a path with an electron depth $\tau_e > 1$. Only collisions with substantial energy loss are considered when computing the electron depth, τ_e (see Section 2.2).

For all three outgassing cases, there are collisional electrons produced when the 3D electric and magnetic fields are used. However, the distribution of these collisional electrons is not uniform throughout the coma. Electrons produced close to the nucleus are more likely to be collisional. Fig. 9 shows the fraction of collisional electrons as a function of the cometocentric distance at which the electron is produced. For example, an electron produced, through photoionization or electron-impact ionization, between 40 and 50 km at an outgassing rate of $Q = 10^{27}\,s^{-1}$ has a 51 per cent chance of following a path with $\tau_e > 1$. At each outgassing rate, the collisional fraction is largest in the inner coma and decreases with cometocentric distance. At outgassing rates of $Q = 5 \times 10^{26}\,s^{-1}$ and $Q = 10^{27}\,s^{-1}$, the collisional fraction of electrons decreases at the innermost radial bin. The electrons produced in the inner bin are more likely to collide with the nucleus, in which case they are removed from the simulation and limiting the electron depth which they can accumulate.

We define the electron cooling exobase as the region below which $1/e$ of the electrons are collisional. It is not required that all the electrons should be collisional, as the cold electron population is still a minor component of the total electron population, of which warm electrons make up the bulk. We fit the collisional fraction with a negative exponential for each outgassing rate (red, Fig. 9). For an outgassing rate of $Q = 5 \times 10^2\,s^{-1}$, the fraction of collisional electrons drops to 35 per cent at a cometocentric distance of 65 km. For $Q = 10^{27}\,s^{-1}$, the cooling exobase extends further out to 105 km. These cometocentric distances agree well with the region of high-cold electron density in Fig. 3. As expected, the electron cooling exobase extends to larger cometocentric distances with increased outgassing rates.

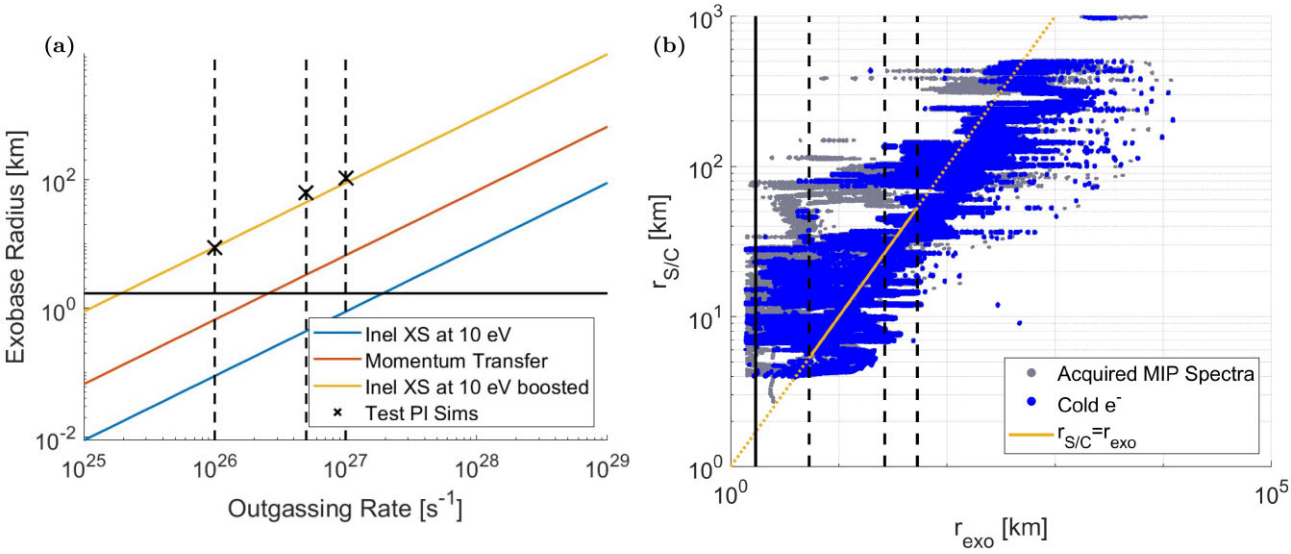

Figure 10. (a) Estimated positions of the electron exobase from equation (1) using $u_{\rm gas} = 1\,{\rm km\,s^{-1}}$ and (blue) the inelastic collision cross section at 10 eV for $E_{\rm Th} > 0.15$ eV, (red) the electron–neutral momentum transfer cross-section (Mandt et al. 2016) and (yellow) the inelastic cross-section boosted by a factor of 100 (equation 7). The horizontal black line is the radius of the nucleus. Vertical dashed lines indicate the outgassing rates used in the test particle simulations. Crosses – estimated position of the electron exobase in the test particle simulations. (b) Cometocentric distance of Rosetta against the new estimate of the electron cooling exobase distance, $r_{\rm exo}$, for the cold electron detections (blue points) by RPC/MIP (Gilet et al. 2020). Grey points are the acquired RPC/MIP spectra without cold electron detections (Gilet et al. 2020). The yellow line indicates where the exobase is at the spacecraft location. Points to the left of the yellow line are not expected to be collisional. The dotted yellow line is used outside the range of outgassing rates modelled here, as the approximation of the exobase position may not be valid. Vertical dashed lines correspond to outgassing rates of the test particle simulations, with $u_{\rm gas} = 1\,{\rm km\,s^{-1}}$ (see Table 1 and equation 7), while the solid black line indicates the nucleus surface.

For the case of radial electron outflow, none of the electrons experienced a large electron depth for any of the outgassing rates, so the collisional electron fraction is 0 throughout the coma. The electron cooling exobase has not formed and no region of the coma should be thought of as collisional.

Fig.10(a) shows the estimated exobase distance based on radial outflow of electrons (red; Mandt et al. 2016), as a function of the outgassing rate. The estimated exobase distance uses the momentum transfer collision cross-section at 5 eV ($\sigma_{\rm mom} = 5 \times 10^{-16}\,{\rm cm^2}$).

In this study, we are focused on the process of electron cooling, through inelastic collisions with the neutral coma. Therefore, it is more relevant to consider the cross-section for inelastic collisions at a typical cometary electron temperature of 10 eV, $\sigma_{\rm inel} = 6.7 \times 10^{-17}\,{\rm cm^2}$. The estimated exobase position using the inelastic collision cross- section and radial outflow is shown in blue. Both of these estimates, neglect the realistic path length followed by electrons in the cometary environment once gyromotion and trapping are included. Based on the exobase radii from the collisional simulations (see Fig. 10), we estimate a factor 100 increase in the collisionality of the coma, due to the complex electron motion. This is consistent with the increase in the electron depth for the collisional tail (range of factor 30 to 130 for the 90th percentile) of the electron distributions in Fig. 8, particularly for the two higher outgassing rates.

Therefore, we propose an estimate of the electron cooling exobase of

$$r_{\rm exo} = 100 \times n_{S/C}\,\sigma_{\rm inel}\,r_{S/C}^2 = \frac{100\,Q\,\sigma_{\rm inel}}{4\pi\,u_{\rm gas}}, \quad (7)$$

where the factor 100 approximates the realistic motion of the electron in the electric and magnetic fields. The cooling exobase estimate, using equation (7), is shown in Fig. 10 (yellow). This enhanced estimate based on the increased path length of the electrons also agrees well with regions of large cold electron fraction in Fig. 5.

We apply this new estimate of the electron cooling exobase to the detections of cold electrons from RPC/MIP (Gilet et al. 2020) throughout the Rosetta mission (see Fig. 10). The estimated exobase location for each cold electron measurement has been corrected using equation (7). Under the assumption of radial outflow, the cold electron observations occurred almost entirely outside the estimated electron exobase, and there were many observations when no exobase was expected to form in the coma (Gilet et al. 2020). With the revised cooling exobase estimate, the cold electron observations are in much better agreement with the expected region of collisionality in the coma (Fig. 10). Notably, very few of the observations occurred when no cooling exobase was expected ($r_{\rm exo} < r_{67P} = 1.7\,{\rm km}$). Therefore, the cold electron observations can be well understood, when the complex electron motion in the magnetic and electric fields are accounted for. Equation (7) gives a good estimate of the region of the coma with collisional electrons, for outgassing rates between $Q = 10^{26}\,{\rm s^{-1}}$ and $Q = 10^{27}\,{\rm s^{-1}}$.

At higher outgassing rates, it is expected that this relationship will break down, as the cold electrons form the bulk electron population and additional plasma boundaries such as the diamagnetic cavity form in the coma. Both of these processes, would substantially alter the electron dynamics in the coma, so the approximation for the increased path length would become invalid.

While there is greatly improved agreement, many of the cold electron observations still occur outside the expected collisional region. There are several key causes that may drive this discrepancy. First, cold electrons may undergo transport from the collisional region, below the cooling exobase, to higher cometocentric distances, where they may be detected by Rosetta. This may be prevalent in the tailward region, where cold electrons were preferentially transported

(see Fig. 6), although Rosetta orbited mostly in the terminator plane. Secondly, the cometary environment is strongly asymmetric, in both the outgassing from the coma and in the electron population. The cooling exobase estimate in equation (7) is based on spherical symmetry in the electron cooling. The impact of the electric and magnetic fields already causes some asymmetry in the exobase, but these sources of asymmetry would lead to further deviation from a spherical exobase surface. The impact of asymmetric outgassing on the collisionality in the coma and electron trapping should be explored in future work.

Finally, the test particle simulations in this study are all subject to a single set of solar wind conditions. At 67P, these conditions varied substantially throughout the mission, and led to variations of several orders of magnitude in the electron-impact ionization frequency (Stephenson et al. 2023). Also, the solar wind variations have been shown to significantly enhance plasma dynamics in the coma, with the generation of local plasma density gradients, not observed with a steady-state solar wind (Behar, E. & Henri, P. 2023). The solar wind variations are therefore likely to impact the magnitude of the ambipolar potential well, and accordingly the efficiency of cometary electron trapping.

5 CONCLUSION

We have demonstrated that trapping of electrons in an ambipolar potential well can cause substantial cooling of electrons, even at very low outgassing rates. A cold electron population is formed at outgassing rates as low as $Q = 10^{26}\,\mathrm{s}^{-1}$, resulting from trapped cometary electrons that have undergone inelastic collisions. The cold electron population is formed mostly close to the nucleus, where the neutral density is high. Once cooled, the electrons are trapped in the potential well parallel to the magnetic field, before being transported downstream and into the tail by an $\boldsymbol{E} \times \boldsymbol{B}$ drift.

The complex electric and magnetic fields, within the coma of a weakly outgassing comet, are crucial to the production of cold electrons. When the realistic electron dynamics are included, cometary electrons are 100 times more collisional than predicted under the previously assumed case of radial outflow. The electrons produced near the nucleus are more collisional and therefore more likely to become cold.

We have revisited the definition of the electron exobase in the coma, given the increased path of the electrons when trapping and gyromotion are accounted for. The new estimate of the electron cooling exobase, informed by the test particle simulations, agrees well with the observations of cold electrons throughout the Rosetta mission by RPC/MIP and RPC/LAP (Engelhardt et al. 2018; Gilet et al. 2020). However, the range of outgassing rates at which the estimate can be applied is limited to $Q = 10^{26}\,\mathrm{s}^{-1}$ to $Q = 10^{27}\,\mathrm{s}^{-1}$. At higher outgassing rates, it is expected that the feedback from collisional processes onto the electric and magnetic fields would become significant and additional plasma boundaries, such as the diamagnetic cavity can form close to the nucleus (Goetz et al. 2016a, b). To model the cold electron population at these higher outgassing rates, it is necessary to incorporate electron–neutral collisions into the Particle-in-Cell model.

Moving forward, the collisional model could be extended to examine the impact of asymmetric outgassing conditions on the cold electron population, which would be more reflective of the conditions at 67P (e.g. Hansen et al. 2016). Additionally, it is unclear how the electron cooling exobase depends on the upstream solar wind conditions, which are likely to be the source of variation in the electron-impact ionization frequencies and subsequently the electron density.

ACKNOWLEDGEMENTS

We gratefully acknowledge the work of the many engineers, technicians, and scientists involved in the Rosetta mission and in the ROSINA and RPC instruments in particular. Without their contributions, ROSINA and RPC would not have produced such outstanding results. Rosetta is an ESA mission with contributions from its member states and NASA. Work at Imperial College has been supported by the Science and Technology Facilities Council (STFC) of the UK under STFC grants ST/S505432/1, ST/SO00364/1, and ST/W001017/1 Work at LPC2E and Lagrange laboratories is co-funded by CNES. JD gratefully acknowledge support from NASA's Rosetta Data Analysis Program, grant no. 80NSSC19K1305. This work was supported in part by NASAs Solar System Exploration Research Virtual Institute (SSERVI): Institute for Modeling Plasmas, Atmosphere, and Cosmic Dust (IMPACT), and the NASA High-End Computing (HEC) Programme through the NASA Advanced Supercomputing (NAS) Division at Ames Research Center.

DATA AVAILABILITY

The data underlying this article will be shared on reasonable request to the corresponding author.

REFERENCES

Bame S. J. et al., 1986, Science, 232, 356
Behar E., Henri P., 2023, A&A, 671, A144
Broiles T. W. et al., 2016a, J. Geophys. Res.: Space Phys., 121, 7407
Broiles T. W. et al., 2016b, MNRAS, 462, S312
Burch J. L., Goldstein R., Cravens T. E., Gibson W. C., Lundin R. N., Pollock C. J., Winningham J. D., Young D. T., 2007, Space Sci. Rev., 128, 697
Carr C. et al., 2007, Space Sci. Rev., 128, 629
Cho H., Park Y., Tanaka H., Buckman S., 2004, J. Phys. B: Atomic, Mol. Optical Phys., 37, 625
Chutjian A., Hall R. I., Trajmar S., 1975, J. Chem. Phys., 63, 892
Clark G. et al., 2015, A&A, 583, A24
Cowley S. W. H., McCrea W. H., Turner G., Hutchison R., Meadows A. J., Pillinger C. T., 1987, Phil. Trans. R. Soc. A, Math. Phys. Sci., 323, 405
Cravens T., 1987, Adv. Space Res., 7, 147
Deca J., Divin A., Henri P., Eriksson A., Markidis S., Olshevsky V., Horányi M., 2017, Phys. Rev. Lett., 118, 205101
Deca J., Henri P., Divin A., Eriksson A., Galand M., Beth A., Ostaszewski K., Horányi M., 2019, Phys. Rev. Lett., 123, 055101
Divin A., Deca J., Eriksson A., Henri P., Lapenta G., Olshevsky V., Markidis S., 2020, ApJ, 889, L33
Engelhardt I. A. D., Eriksson A. I., Vigren E., Valières X., Rubin M., Gilet N., Henri P., 2018, A&A, 15
Eriksson A. I. et al., 2007, Space Sci. Rev., 128, 729
Eriksson A. I. et al., 2017, A&A, 605
Faure A., Gorfinkiel J., Tennyson J., 2004, J. Phys. B: Atomic, Mol. Opt. Phys., 37, 801
Galand M. et al., 2016, MNRAS, 462, S331
Gan L., Cravens T. E., 1990, J. Geophys. Res.: Space Phys., 95, 6285
Gilet N., Henri P., Wattieaux G., Cilibrasi M., Béghin C., 2017, Radio Sci., 52, 1432
Gilet N. et al., 2020, A&A, 640, A110
Goetz C. et al., 2016a, MNRAS, 462, S459
Goetz C. et al., 2016b, A&A, 588, A24
Gulkis S. et al., 2015, Science, 347, aaa0709
Hansen K. C. et al., 2016, MNRAS, 462, stw2413
Heritier K. L. et al., 2017, MNRAS, 469, S427

Heritier K. L. et al., 2018, A&A, 618, A77
Itikawa Y., Mason N., 2005, J. Phys. Chem. Ref. Data, 34, 1
Körösmezey A. et al., 1987, J. Geophys. Res., 92, 7331
Krankowsky D. et al., 1986, Nature, 321, 326
Madanian H. et al., 2016, J. Geophys. Res.: Space Phys., 121, 5815
Mandt K. E. et al., 2016, MNRAS, 462, S9
Meyer-Vernet N., Couturier P., Hoang S., Perche C., Steinberg J., Fainberg J., Meetre C., 1986, Science, 232, 370
Myllys M. et al., 2019, A&A
Nilsson H. et al., 2022, A&A, 659, A18
Rème H. et al., 1986, Nature, 321, 349
Shapiro V. D., Bingham R., Dawson J. M., Dobe Z., Kellett B. J., Mendis D. A., 1999, J. Geophys. Res.: Space Phys., 104, 2537
Simon Wedlund C. et al., 2019, A&A
Sishtla C. P., Divin A., Deca J., Olshevsky V., Markidis S., 2019, Phys. Plasmas, 26, 102904
Stephenson P., Galand M., Deca J., Henri P., Carnielli G., 2022, MNRAS, 511, 4090
Stephenson P. et al., 2023, MNRAS, 525, 5041
Thomsen M. F., Bame S. J., Feldman W. C., Gosling J. T., McComas D. J., Young D. T., 1986, Geophys. Res. Lett., 13, 393
Trotignon J. G. et al., 2007, Space Sci. Rev., 128, 713
Wattieaux G., Henri P., Gilet N., Vallières X., Deca J., 2020, A&A, 638, A124
Zwickl R. D., Baker D. N., Bame S. J., Feldman W. C., Fuselier S. A., Huebner W. F., McComas D. J., Young D. T., 1986, Geophys. Res. Lett., 13, 401

This paper has been typeset from a TEX/LATEX file prepared by the author.